Application of Takens's Delay-Embedding to extract indirect measurements from nonlinear oscillating sensors

Francesco Grimaldi[1], Christian Geminiani[1] and Andrea Tilli[1]

***Abstract*— This paper presents a general procedure for extracting a physical measurand from the output of oscillating or periodically forced sensors, such as mechanical MEMS resonators and electrical or electromagnetic LC/RLC devices. The sensor together with its excitation is modeled as an autonomous dynamical system in which the measurand acts as a slowly varying state, while the excitation is parameterized by a phase variable. Under suitable smoothness and observability assumptions, Takens' delay-embedding theorem guarantees the existence of an injective map from the low-dimensional state space to a higher-dimensional space of delayed output samples, thereby enabling a deadbeat-like reconstruction through an approximate inverse map.**

Jacobian-based indicators are introduced to verify the necessary condition of local invertibility of this map and to assess the conditioning of the resulting output manifold. The inverse reconstruction map is then approximated through neural-network-based function approximation trained on synthetic data generated from the autonomous model.

The proposed methodology is illustrated through a temperature-dependent RLC benchmark under different capacitance–temperature laws. The results highlight the potential of this approach as an indirect sensing strategy for a broad class of oscillating sensors.

I. INTRODUCTION

Oscillating and periodically forced sensors constitute a broad class of transducers in which the quantity of interest is encoded in the dynamic response of a mechanical, electrical, or electromagnetic resonator. In these architectures, the measurand modulates properties such as resonant frequency, quality factor, or steady-state amplitude, which can be read with very high accuracy by frequency- or phase-tracking circuits. These quantities are also naturally suited to digital processing and wireless interrogation.

From a dynamical point of view, two main categories can be distinguished. A first class comprises truly self-oscillating sensors, whose natural oscillation frequency is shifted by the measurand and continuously tracked by a sustaining oscillator loop. Typical examples include atomic and nuclear-magnetic-resonance magnetometers, where the quantity of interest, for instance the magnetic field, is encoded in the Larmor precession frequency of an ensemble of spins and read out by frequency- or phase-tracking electronics [1], [2].

*This work was not supported by any organization

[1]Francesco Grimaldi, Christian Geminiani and Andrea Tilli are with the Department of Electrical, Electronic and Information Engineering (DEI). Alma Mater Studiorum – University of Bologna (UniBo). francesco.grimaldi6@unibo.it

A second class comprises sensors that possess resonant characteristics but are driven by an external source and forced to oscillate at the excitation frequency; in this case the measurand appears in the amplitude, phase, or higher-harmonic content of the forced response. This category includes quartz and SAW resonator sensors [3], wireless passive LC or RFID-like tags for harsh environments [5], [4], and, more specifically, MEMS vibratory gyroscopes [6], as well as inductive arrangements such as metal detectors and magnetic-field probes.

In all these cases, the transduction chain is typically highly nonlinear, and the mapping from the measured dynamic signal to the underlying physical quantity can be complex, especially when large oscillation amplitudes, strong coupling, or operation in harsh environments are involved. The resulting reconstruction usually relies on detailed analytical, observation-oriented models, that is, tractable in terms of complexity and state dimension, and on sensor-specific algorithm design, often supported by extensive calibration tables or *ad hoc* linearisation. Such approaches are difficult to generalise across sensor types.

In view of these limitations, the objective of this work is to propose a general procedure that can be applied to a wide family of oscillating sensors, mechanical or electrical, resonant or periodically forced, without sensor-specific reconstruction algorithm design. The key idea is to exploit the Takens delay-embedding framework [7] to generate a deadbeat-like observer [8], [9] of the state. To this end, the sensor and its excitation are first described by a single dynamical model, obtained by embedding the excitation mechanism into the sensor equations, so as to obtain an overall autonomous system. In the latter, the measurand acts as a slowly varying state and the excitation is parameterized by a master phase variable. Under suitable smoothness and observability conditions [10], the Takens delay-embedding theorem guarantees the existence of an information-preserving injective map, that is, an embedding [11], from the low-dimensional state into a higher-dimensional Euclidean space of time-delayed output samples.

Exploiting this property, a direct, that is, deadbeat-like, reconstruction of the current state can be obtained by applying the inverse of the above-mentioned map to a suitable vector of delayed measured outputs. In general, analytical derivation of such forward and inverse maps is intractable, even for relatively simple systems with few states. Consequently, sample-based function approximation methods are employed in the present work. Radial Basis Function (RBF) neural networks are a natural choice in this context: they approximate nonlinear maps as linear combinations of localized, distance-based units, typically Gaussian, offering universal approximation with relatively few neurons in low-dimensional settings and enabling simple, well-conditioned training of the linear output weights [12], [13]. Their locality can become costly in high-dimensional spaces, where it is often preferable to resort to deeper architectures that increase network depth rather than excessively widening a single RBF layer. Therefore, a feedforward neural-network approach is exploited to approximate the state-reconstructing function. For its training, following synthetic-data approaches, multiple simulations of the sensor together with its excitation are properly arranged, avoiding the need for large sets of experimental data.

It is worth noting that the model used for data generation need not be a low-complexity model tailored to dynamic-observer development. Even high-dimensional, sophisticated representations, such as FEM-based models, can be adopted, provided that the hypothesis of an underlying low-dimensional, smooth, observable dynamics holds, even if its equations are unknown in closed form. The above-mentioned procedure can thus be applied to any sensor belonging to the considered category without any design step specifically tailored to the given application.

To illustrate the proposed indirect sensing methodology, the framework is applied to a temperature-dependent series RLC circuit operating as an oscillating electrical sensor. The benchmark is analyzed under both linear and hyperbolic capacitance-temperature laws, in order to show how the physical transduction law affects observability, output-manifold conditioning, and reconstruction performance.

The paper is organized as follows. Section II first introduces typical dynamical models for resonator-based sensors, covering both self-oscillating and externally forced configurations within a unified formulation. Section III then develops a nonlinear, deadbeat-like state-reconstruction strategy based on time-delay embedding and neural networks exploited as function approximators. Since observability is a critical issue, a procedure is proposed to quantify how sensitive the output is to variations of the target parameter p. This can be used to guarantee the necessary conditions for inverse-mapping reconstruction and to guide the sensor design process. Finally, Section IV illustrates the overall workflow on a temperature-dependent RLC benchmark under different capacitance laws.

II. Typical Resonator Models

As discussed in the Introduction, oscillating sensors can be divided into two main categories:

- *Self-oscillating active sensors*: they have no forcing input and exhibit a natural oscillation in the form of a limit cycle in the phase plane, whose shape depends on the value of the target variable.
- *Forced-oscillating sensors*: they are passive systems driven by an external oscillating signal and typically exhibit a damped resonance that depends on the value of the target variable. The frequency of the exciting signal is commonly chosen within the resonance range so as to maximize sensitivity. These sensors usually converge rapidly to an attractive oscillating steady-state behavior associated with the forcing signal.

Both classes are described by a small set of variables, whose roles and admissible domains are specified here. Time is denoted by $t \in \mathbb{R}_{\geq 0}$. The target variable to be reconstructed is denoted by $p(t)$, and is assumed to be a real-valued scalar variable belonging to a compact admissible interval

$$p(t) \in \mathcal{P} = [p_{\min}, p_{\max}] \subset \mathbb{R} \tag{1}$$

Depending on the application, p may represent a temperature, an angular rate, a magnetic field, or another physical measurand. No positivity assumption is imposed in the general formulation, unless required by the specific physical case. Since p is assumed to vary slowly with respect to the oscillatory sensor dynamics, it is regarded as constant over the time scale of the reconstruction window:

$$\dot{p}(t) = 0 \tag{2}$$

The oscillatory component is represented by

$$w(t) = \begin{bmatrix} w_1(t) \\ w_2(t) \end{bmatrix} \in \mathbb{R}^2 \tag{3}$$

where $w_1(t)$ and $w_2(t)$ are real-valued bounded quadrature components of the oscillation. The initial condition is chosen such that $\|w(0)\|_2 = 1$, so that $w(t)$ evolves on the unit circle $\mathbb{S}^1$ under the oscillator dynamics introduced below. The measured output is denoted by $y(t) \in \mathbb{R}$ and corresponds to the scalar signal available for state reconstruction. The associated output map is assumed to be sufficiently smooth on its domain.

A. Self-oscillating active sensor model

A self-oscillating sensor can be represented by:

$$\dot{w}(t) = S\, w(t) = \begin{bmatrix} 0 & -\omega(p) \\ \omega(p) & 0 \end{bmatrix} \begin{bmatrix} w_1(t) \\ w_2(t) \end{bmatrix} \tag{4}$$

$$\|w(0)\|^2 = 1 \tag{5}$$

$$y = h(w, p) \tag{6}$$

The constraint on the initial condition forces the dynamics of w to remain on the unit circle in the phase plane.

B. Forced-oscillating sensor model

For a forced-oscillating sensor, let

$$u = \text{oscillating sensor input} \tag{7}$$

The excitation can be described by

$$\dot{w}(t) = S\, w(t) = \begin{bmatrix} 0 & -\omega \\ \omega & 0 \end{bmatrix} \begin{bmatrix} w_1(t) \\ w_2(t) \end{bmatrix} \tag{8}$$

$$\|w(0)\|^2 = 1 \tag{9}$$

$$u = u(w) \tag{10}$$

The forced sensor itself is described by

$$\dot{x}(t) = f(x, p, u) \tag{11}$$

$$y = h(x, p) \tag{12}$$

In order to be effective, forced resonators are designed so that the system state space X, with elements

$$\chi = \begin{bmatrix} x & p & w \end{bmatrix}^\top \tag{13}$$

admits an attractive invariant graph. Any trajectory originating outside this manifold is attracted to it. Such an invariant can be defined by a smooth mapping:

$$x = \Pi(w, p) \tag{14}$$

This function effectively constrains the driven variables x to the driving dynamics (w, p). Usually, by design, the convergence rate to the invariant graph is imposed to be fast with respect to the forcing oscillation period $2\pi/\omega$ [14]. Consequently, the system can be rewritten in reduced form as

$$\dot{w}(t) = S\, w(t) = \begin{bmatrix} 0 & -\omega(p) \\ \omega(p) & 0 \end{bmatrix} \begin{bmatrix} w_1(t) \\ w_2(t) \end{bmatrix} \tag{15}$$

$$\|w(0)\|^2 = 1 \tag{16}$$

$$x(t) = \Pi(w, p) \tag{17}$$

$$y = h(\Pi(w, p), p) = h(w, p) \tag{18}$$

C. Unified oscillating sensor model

From (4) and (15), it follows that both sensor classes can be analyzed within a single framework:

$$\dot{p}(t) = 0 \tag{19}$$

$$\dot{w}(t) = S\, w(t) = \begin{bmatrix} 0 & -\omega(p) \\ \omega(p) & 0 \end{bmatrix} \begin{bmatrix} w_1(t) \\ w_2(t) \end{bmatrix} \tag{20}$$

$$\|w(0)\|^2 = 1 \tag{21}$$

$$y = h(w, p) \tag{22}$$

Here, in the case of forced-oscillating sensors, ω is actually independent of the target variable p. In the following, it is assumed that the sensor-excitation system satisfies the structural conditions required by the proposed method, namely sufficient smoothness of the dynamics and of the output map, together with local observability, understood as state distinguishability from the output trajectories [15]. These properties are assumed to be ensured at the design stage of the sensor, so that the resulting autonomous model belongs to the class of systems to which the subsequent delay-embedding and reconstruction procedure can be applied.

III. Nonlinear Deadbeat-Like Reconstruction via Neural-Network Approximation

In light of the unified resonator model, the main difficulty lies in the output static function $h(w, p)$, which may take an arbitrary form and thus makes observer design difficult. By exploiting the fact that, on the invariant limit cycle, the oscillatory state

$$w = \begin{bmatrix} w_1(t) & w_2(t) \end{bmatrix}^\top$$

evolves on a one-dimensional manifold, it is convenient to re-parameterize w by means of a single phase-angle state $\vartheta(t)$. In this way, the redundant two-dimensional description is replaced by a scalar variable that uniquely identifies the position along the orbit, reducing the state dimension and making the periodic structure of the dynamics explicit. This yields an overall autonomous second-order model with state belonging to a compact set.

$$x = (\vartheta, p) \tag{23}$$

Thanks to the observability assumptions stated at the end of Section II, the Takens embedding framework [7] guarantees that the state vector (ϑ, p) can be reconstructed from a stack of $2n+1$ samples of the output response, where n is the number of states of the system, provided that a suitable sampling period T_s is selected in accordance with the dynamical characteristics of the sensor. Since both ϑ and p are scalar variables, the number of required samples is five.

Therefore, it is possible to define the output vector-valued function H of the sensor model, which maps the domain X of all possible state coordinates, a subset of $\mathbb{R}^2$, into the output manifold $Y \subset \mathbb{R}^5$:

$$\mathbf{y}(t) = \begin{bmatrix} y(t) \\ y(t+T_s) \\ y(t+2T_s) \\ y(t+3T_s) \\ y(t+4T_s) \end{bmatrix} = \begin{bmatrix} h(\vartheta(t), p) \\ h(\vartheta(t+T_s), p) \\ h(\vartheta(t+2T_s), p) \\ h(\vartheta(t+3T_s), p) \\ h(\vartheta(t+4T_s), p) \end{bmatrix} \tag{24}$$

The output function H can be characterized through repeated simulations of the sensor system, collecting the resulting state-output pairs in a look-up-table-like form. By feeding this dataset to a suitable neural-network function approximator, it becomes possible to approximate the vector-valued inverse function H^{-1}, which represents the reconstruction mapping. In order to guarantee such reconstruction, the system must be observable. This property has been assumed to be ensured by design. Nevertheless, low sensitivity of the output sample vector to state variations can impair the effectiveness of the proposed approach. For this reason, the next subsection introduces a dedicated sensitivity analysis.

A. Local invertibility as a necessary condition

According to the Takens framework, a necessary condition for state observability is the local invertibility of the observation map $H : X \to Y$, that is, local observability of the system. In differential terms, this requires that the Jacobian matrix of H have full column rank at every point $x \in X$. Its columns span the tangent plane to the output manifold $H(X)$. The full-column-rank condition ensures that this tangent plane is genuinely two-dimensional and does not collapse onto a line or a point. This can be interpreted as a proper local inclination of the output manifold at each of its points, so that small perturbations in each state direction produce distinguishable variations in the output.

To exploit the above consideration from a practical viewpoint, an approximation of the Jacobian matrix of $H(\vartheta, p)$ can be computed and the full-column-rank condition can be checked numerically. Specifically, a small finite variation $\delta\vartheta$ is applied to the phase coordinate, and the resulting incremental changes in each of the five scalar components of the output stack are collected into a vertical sensitivity vector. The same procedure is repeated for the parameter p with a small absolute variation δp. The two sensitivity vectors then represent the numerical columns of the Jacobian approximation:

$$\frac{\partial H}{\partial x}(\vartheta(t), p) = \begin{bmatrix} \frac{\partial H}{\partial \vartheta} & \frac{\partial H}{\partial p} \end{bmatrix} = \begin{bmatrix} \frac{\partial h_1}{\partial \vartheta} & \frac{\partial h_1}{\partial p} \\ \frac{\partial h_2}{\partial \vartheta} & \frac{\partial h_2}{\partial p} \\ \frac{\partial h_3}{\partial \vartheta} & \frac{\partial h_3}{\partial p} \\ \frac{\partial h_4}{\partial \vartheta} & \frac{\partial h_4}{\partial p} \\ \frac{\partial h_5}{\partial \vartheta} & \frac{\partial h_5}{\partial p} \end{bmatrix} \tag{25}$$

It is then numerically verified that the two column vectors are both non-null and linearly independent. The non-null condition is quantified through the norms of both vectors, which are required to remain above a prescribed threshold. Linear independence of the two columns of the approximated Jacobian is assessed by means of a normalized collinearity indicator, defined from the orthogonal component of one column with respect to the other. This indicator takes values between 0 (perfect collinearity) and 1 (near orthogonality); values sufficiently above a chosen threshold are interpreted as practical evidence of linear independence and thus of a locally full-rank Jacobian.

The proposed indicators are not only diagnostic but also provide a practical tool for sensor design. In particular, the norms of the Jacobian columns and the normalized collinearity measure can be evaluated over the admissible design space, for instance excitation frequency, component values, and operating range, to identify parameter combinations that maximize sensitivity while avoiding near-degenerate regions. In this way, the same numerical machinery used to certify local observability can be exploited in a systematic design phase, guiding the tuning of the sensor and excitation parameters toward configurations that enhance the conditioning of the output manifold and, ultimately, improve the robustness and accuracy of the state reconstruction.

B. *Neural-network function reconstruction*

As already mentioned, the final step consists of approximating the pseudoinverse function that recovers the state variables from the measured delay vector. To this end, the collected dataset is used to train a Radial Basis Function neural network, chosen for its ability to approximate smooth nonlinear functions with high accuracy [12], [13]. RBF neural networks are a natural choice in this context because they represent nonlinear maps as linear combinations of localized, distance-based units, typically Gaussian, and therefore offer universal approximation with relatively few neurons in low-dimensional settings. Moreover, once centers and widths are fixed, the linear output weights can be trained in a simple and well-conditioned way. Their locality can become costly in high-dimensional spaces, but this limitation is not critical here, since the embedded state remains low-dimensional.

The network must be trained with a sufficiently dense set of samples and a strict error tolerance, so that it captures the essential nonlinear structure of the inverse map while maintaining satisfactory generalization capability. Once calibrated, the neural network can be embedded into the deadbeat-observer framework to provide real-time estimation of the state variables from measured output stacks, thereby enabling indirect measurement of the target physical parameter p.

IV. RLC Benchmark as an Illustrative Example

To illustrate the proposed framework, a temperature-dependent series RLC circuit is used as a simple but representative forced-oscillation benchmark. The measurand affects the resonant response through the capacitance $C(T)$, while the measured output is the voltage across one resistor. This setting preserves a clear physical interpretation and allows the effect of different capacitance-temperature laws on observability, output-manifold conditioning, and estimation accuracy to be compared.

The system consists of a lumped series RLC circuit, whose capacitance depends on temperature. For convenience, a sinusoidal excitation voltage is assumed to be directly applied to the circuit, while the single measured output is taken as the voltage across one resistor, which is a scaled representation of the circuit current. This configuration provides a simple forced-oscillation sensor in which the measurand affects the steady-state oscillatory response through the temperature dependence of the capacitance. The input voltage is assumed to be sinusoidal, with fixed amplitude and frequency. Neglecting the transient response and focusing on the steady-state oscillatory regime, the signal generator can be embedded into the system model, thus obtaining an autonomous augmented representation whose effective state variables are the oscillation phase and the temperature. The resulting output voltage will then serve as the unique measured quantity from which the temperature information is reconstructed.

A. *Temperature-Dependent RLC State-Space Model*

The analytical model of the benchmark RLC circuit is derived so as to provide a theoretical reference for validating

TABLE I

Main quantities used in the temperature-dependent RLC benchmark.

Symbol	Domain/unit	Role
Target variable and dependent quantity		
$T(t)$	$\mathcal{T} \subset \mathbb{R}$ [°C]	Target temperature, constant over one window.
$C(T)$	$\mathbb{R}_{>0}$ [F]	Temperature-dependent capacitance.
Time-dependent variables		
$\vartheta(t)$	$[0, 2\pi)$ [rad]	Excitation phase.
$v_{\mathrm{in}}(t)$	$\mathbb{R}$ [V]	Input voltage.
$i(t)$	$\mathbb{R}$ [A]	Series current.
$v_C(t)$	$\mathbb{R}$ [V]	Capacitor voltage.
$v_{\mathrm{out}}(t) = y(t)$	$\mathbb{R}$ [V]	Measured output across R_2.
$w(t)$	$\mathbb{S}^1 \subset \mathbb{R}^2$	Exosystem state.
Constant system parameters		
V_{cc}	$\mathbb{R}_{>0}$ [V]	Input amplitude.
ω_0, f_0	$\mathbb{R}_{>0}$ [rad/s], [Hz]	Excitation frequency, $\omega_0 = 2\pi f_0$.
L	$\mathbb{R}_{>0}$ [H]	Lumped inductance.
R_1, R_2	$\mathbb{R}_{>0}$ [Ω]	Lumped resistances.
C_0	$\mathbb{R}_{>0}$ [F]	Capacitance-law parameter.
k_c	law-dependent	Capacitance-law gain.
T_0	$\mathbb{R}$ [°C]	Reference or virtual singularity.

the proposed estimation framework. The adopted quantities are grouped in Table I. Using the circuit current and the capacitor voltage as state variables, and the voltage across R_2 as measured output, the input, state, and output variables are defined as

$$\begin{aligned} u(t) &= v_{\mathrm{in}}(t) \\ x(t) &= \begin{bmatrix} x_1(t) \\ x_2(t) \end{bmatrix} = \begin{bmatrix} i(t) \\ v_C(t) \end{bmatrix} \\ y(t) &= v_{\mathrm{out}}(t) = R_2 i(t) = R_2 x_1(t) \end{aligned} \tag{26}$$

For each fixed temperature value T, the temperature-dependent RLC dynamics can then be written as follows.

$$\dot{x}(t) = A(T)x(t) + Bu(t) \qquad y(t) = Cx(t)$$

$$A(T) = \begin{bmatrix} -\dfrac{R_1 + R_2}{L} & -\dfrac{1}{L} \\ \dfrac{1}{C(T)} & 0 \end{bmatrix} \quad B = \begin{bmatrix} \dfrac{1}{L} \\ 0 \end{bmatrix} \quad C = \begin{bmatrix} R_2 & 0 \end{bmatrix}$$

To express the sinusoidal excitation in a form consistent with the autonomous framework adopted throughout the paper, the input voltage is generated by the following two-dimensional exosystem:

$$\dot{w}(t) = Sw(t) = \begin{bmatrix} 0 & -\omega_0 \\ \omega_0 & 0 \end{bmatrix} \begin{bmatrix} w_1(t) \\ w_2(t) \end{bmatrix} \tag{27}$$

$$v_{in}(t) = V_{cc}Ew(t) = V_{cc} \begin{bmatrix} 1 & 0 \end{bmatrix} \begin{bmatrix} w_1(t) \\ w_2(t) \end{bmatrix} \tag{28}$$

$$E = \begin{bmatrix} 1 & 0 \end{bmatrix} \tag{29}$$

For a suitable initial condition, namely $\|w(0)\|^2 = 1$, the exosystem generates

$$w(t) = \begin{bmatrix} \cos(\omega_0 t) \\ \sin(\omega_0 t) \end{bmatrix} \qquad v_{in}(t) = V_{cc}\cos(\omega_0 t) \tag{30}$$

By stacking the plant state $x(t)$ and the exosystem state $w(t)$ into the augmented state $\xi(t)$, the sensor together with its excitation can be written as a single autonomous system.

$$\xi(t) = \begin{bmatrix} x(t) \\ w(t) \end{bmatrix} \tag{31}$$

$$\dot{\xi}(t) = \begin{bmatrix} A(T) & BV_{cc}E \\ 0 & S \end{bmatrix} \xi(t) \tag{32}$$

$$y(t) = \begin{bmatrix} C & 0 \end{bmatrix} \xi(t) \tag{33}$$

For each fixed temperature T, the steady-state response to the sinusoidal excitation generated by the exosystem can be sought in the following form, where $\Pi(T)$ is a constant matrix to be determined.

$$x_{ss}(t) = \Pi(T)\, w(t) \qquad \Pi(T) \in \mathbb{R}^{2\times 2} \tag{34}$$

$$\dot{x}_{ss}(t) = \Pi(T)\dot{w}(t) = \Pi(T)Sw(t) \tag{35}$$

$$\dot{x}_{ss}(t) = A(T)x_{ss}(t) + Bv_{in}(t) \tag{36}$$

$$\dot{x}_{ss}(t) = A(T)\Pi(T)w(t) + BV_{cc}Ew(t) \tag{37}$$

Requiring these two expressions to coincide for all trajectories $w(t)$ leads to the Sylvester equation

$$A(T)\Pi(T) - \Pi(T)S = -BV_{cc}E. \tag{38}$$

Under the standard non-resonance condition that the spectra of $A(T)$ and S do not intersect [16], (38) admits a unique solution $\Pi(T)$. The corresponding steady-state output can then be written as

$$y_{ss}(t) = Cx_{ss}(t) = C\Pi(T)w(t) \tag{39}$$

$$v_{out}(t) = \begin{bmatrix} R_2 & 0 \end{bmatrix} \Pi(T) \begin{bmatrix} \cos(\omega_0 t) \\ \sin(\omega_0 t) \end{bmatrix} \tag{40}$$

$$\Pi(T) = \begin{bmatrix} \pi_{11}(T) & \pi_{12}(T) \\ \pi_{21}(T) & \pi_{22}(T) \end{bmatrix} \tag{41}$$

$$v_{out}(t) = R_2 \Big(\pi_{11}(T)\cos(\omega_0 t) + \pi_{12}(T)\sin(\omega_0 t) \Big) \tag{42}$$

$$v_{out}(t) = R_2\, |I_p(T)| \cos\big(\omega_0 t + \varphi(T)\big) \tag{43}$$

$$v_{out}(t) = R_2\, |Y(j\omega_0, T)|\, V_{cc} \cos\big(\omega_0 t + \arg Y(j\omega_0, T)\big)$$

where $Y(j\omega_0, T)$ is the complex admittance of the circuit at angular frequency ω_0 and temperature T. This shows that the steady-state representation obtained via the exosystem and Sylvester equation is fully consistent with the classical harmonic-response description.

Finally, to complete the temperature-dependent model, two alternative constitutive laws are considered for the capacitance. The first one is the linear law,

$$C_{\mathrm{lin}}(T) = C_0 + k_c\,(T - T_0) \tag{44}$$

where C_0 is the capacitance at the reference temperature T_0 and k_c is the linear temperature coefficient. This law provides a baseline model with approximately uniform sensitivity and is consistent with the behavior of stable Class 1 ceramic dielectrics such as NP0/C0G capacitors, whose capacitance exhibits a nearly linear dependence on temperature over the operating range [17].

The second one is a hyperbolic law, written as

$$C_{\mathrm{hyp}}(T) = C_0 + \frac{k_c}{T - T_0} \tag{45}$$

where, in this case, C_0 represents an asymptotic capacitance offset, k_c governs the curvature of the law, and T_0 is a virtual singularity temperature deliberately placed outside the operating interval. This choice guarantees that $C(T)$ remains smooth and positive over the whole temperature range while introducing a stronger and less symmetric nonlinear dependence on temperature than the linear model.

From the methodological viewpoint, the two laws are therefore used here as two numerically distinct alternatives to investigate how the constitutive dependence $C(T)$ affects output-manifold conditioning and inverse reconstruction performance.

B. Data Collection, Observability Analysis, and Neural Reconstruction

For each of the two capacitance–temperature laws introduced above, a separate synthetic dataset is generated over the same rectangular state domain. In particular, a total of $N_T = 100$ temperature values are uniformly selected in the interval

$$T \in [T_{\min}, T_{\max}] = [350^\circ\mathrm{C},\, 550^\circ\mathrm{C}] \tag{46}$$

while $N_\vartheta = 100$ excitation-phase values are uniformly distributed over $\vartheta \in [0, 2\pi)$. This choice yields, for each capacitance law, a grid of $N_{\text{states}} = N_T N_\vartheta = 10^4$ state points. Therefore, two distinct datasets are constructed: one associated with the linear capacitance law and one associated with the hyperbolic capacitance law, each consisting of 10^4 simulated state–output samples.

The considered temperature interval is representative of high-temperature industrial and energy environments in which conventional wireless temperature sensors, typically requiring on-board electronics, are difficult or impossible to deploy.

For each state (ϑ, T) of each dataset, the corresponding stack of delayed output samples is computed according to the observation map H introduced in Section III. In this way, two output manifolds are obtained, one for the linear capacitance law and one for the hyperbolic law, so that their geometrical properties can be compared directly under the same state-domain sampling.

To assess local invertibility of the observation map and, more generally, the conditioning of the two output manifolds, the Jacobian-based indicators introduced in Section III are evaluated numerically over the entire state grid. In both cases, finite-difference approximations are computed by adopting the same absolute perturbations

$$\delta\vartheta = 10^{-3}\ \mathrm{rad} \qquad \delta T = 10^{-3}\ ^\circ\mathrm{C} \tag{47}$$

This allows the norms of the two Jacobian columns and the normalized collinearity indicator to be evaluated for every sampled state, thus providing a quantitative basis for comparing the observability properties induced by the two capacitance laws.

Two sets of fixed system and operating parameters are adopted, one for each capacitance law. They are reported in Table II. The different numerical values are intentionally selected to obtain well-conditioned output manifolds for the two constitutive laws, while preserving the same reconstruction workflow. In both cases, T_s denotes the sampling time used to construct the delayed output vector, whereas f_0 defines the frequency of the sinusoidal excitation. The coefficient k_c has different physical units in the two cases because it belongs to two different capacitance-temperature laws.

TABLE II

System and operating parameters used for the two RLC benchmark simulations.

Parameter	**Unit**	$\mathcal{P}_{\mathrm{lin}}$	$\mathcal{P}_{\mathrm{hyp}}$
V_{cc}	V	40	5
f_0	Hz	$7.12 \cdot 10^5$	$8.12 \cdot 10^5$
L	H	10^{-9}	$5 \cdot 10^{-6}$
R_1	Ω	10^{-4}	1
R_2	Ω	$2 \cdot 10^{-4}$	4
C_0	F	10^{-6}	$2 \cdot 10^{-9}$
k_c	law-dependent	$5 \cdot 10^{-9}\ \mathrm{F}/^\circ\mathrm{C}$	$2.4 \cdot 10^{-6}\ \mathrm{F} \cdot {}^\circ\mathrm{C}$
T_0	°C	450	150
T_s	s	$2.34 \cdot 10^{-7}$	$1.54 \cdot 10^{-7}$

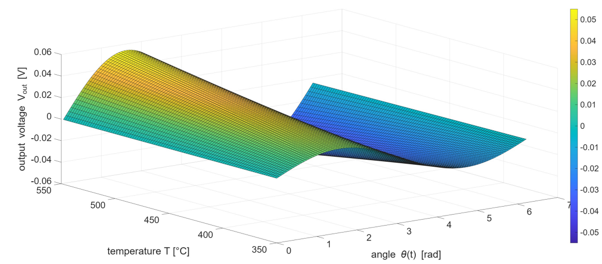

Fig. 1. *Surface of the first output-voltage sample over the state rectangle. Linear capacitance-temperature law.*

As a first simulation result, the first scalar component of the delayed output vector is plotted as a three-dimensional surface over the state rectangle for each of the two capacitance laws. These two plots provide an immediate qualitative visualization of how the output voltage varies with both phase and temperature, and already offer a first visual indication of the different geometrical conditioning of the associated output manifolds. More precisely, the altitude of each surface corresponds to the first sampled output voltage associated with the state coordinate (ϑ, T) on the base plane. Two separate figures are therefore obtained: one for the linear law and one for the hyperbolic law.

After this preliminary observability assessment, the state–output pairs generated for each capacitance law are used to train two separate neural approximators of the inverse map. More precisely, one neural network is trained on the dataset associated with the linear capacitance law, while a

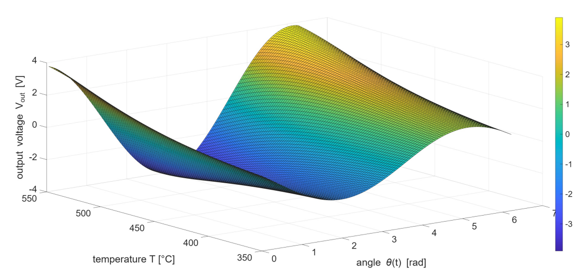

Fig. 2. *Surface of the first output-voltage sample over the state rectangle. Hyperbolic capacitance-temperature law.*

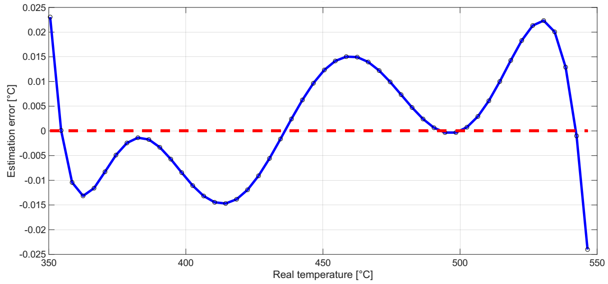

Fig. 3. *Temperature estimation error over the test set for the neural network trained on the linear capacitance-temperature law.*

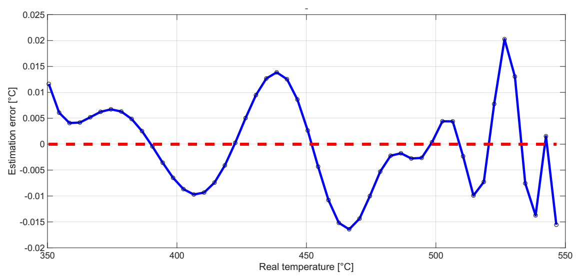

Fig. 4. *Temperature estimation error over the test set for the neural network trained on the hyperbolic capacitance-temperature law.*

second one is trained on the dataset associated with the hyperbolic law. In both cases, the training set consists of the corresponding 10^4 simulated samples.

The inverse map $H^{-1} : \mathbb{R}^5 \to \mathbb{R}^2$ is approximated in MATLAB using `feedforwardnet`. The network input is the five-dimensional delayed output vector, and the output is the estimated state $(\hat{\vartheta}, \hat{T})$. For both capacitance laws, the same architecture is used: three hidden layers with 50, 20, and 10 neurons. The hidden-layer transfer functions are set to `radbas`, whereas the output layer uses `purelin`. All remaining settings, including initialization, preprocessing, data division, training algorithm, performance function, and stopping criteria, are left at the default MATLAB values for `feedforwardnet`. This ensures that the two tests differ only in the generated datasets associated with the two capacitance-temperature laws.

After training, two separate sets of 2500 test samples were generated, one for each capacitance law, corresponding to pairs (ϑ, T) with values slightly different from those used for training but lying within the same operating range. These test sets were used to evaluate the performance of the constructed state observers, in particular with respect to the extraction of the temperature value, i.e. the target variable, from the measured output of the physical system. In this way, the final comparison between the two cases can be carried out not only in terms of output-manifold conditioning, but also in terms of actual temperature-estimation accuracy achieved by the corresponding learned inverse maps.

V. Conclusions

This work presented a Takens-style delay-embedding framework for indirect sensing in oscillating systems. The target variable is reconstructed from delayed samples of a single scalar output by learning an approximate inverse map through a feedforward neural network with radial-basis hidden units. In the temperature-dependent RLC benchmark, tested under both linear and hyperbolic capacitance-temperature laws, the method achieved sub-degree estimation accuracy, supporting the feasibility of the proposed deadbeat-like reconstruction strategy.

The proposed Jacobian-based indicators quantify local invertibility and output-manifold conditioning, and can support sensor design by scanning excitation frequencies, component values, and operating ranges. Since the data-generating model need not be analytically tractable, the workflow can be extended to high-dimensional or FEM-based models when an underlying low-dimensional, smooth, and observable dynamics exists. Future work will address robustness to uncertainties and measurement noise, as well as validation on more realistic oscillating sensors.

References

[1] Kitching, J. E.; Knappe, S.; Donley, E. A. Atomic sensors–a review. *IEEE Sens. J.* **2011**, *11*, 1749–1758. doi:10.1109/JSEN.2011.2157679.

[2] Guo, T.; He, W.; Wan, C.; Zhang, Y.; Xu, Z. NMR magnetometer based on dynamic nuclear-polarization for low-strength magnetic field measurement. *Sensors* **2023**, *23*, 4663. doi:10.3390/s23104663.

[3] Scipioni, A.; Rischette, P.; Santori, A. Wireless surface acoustic wave resonator sensors: Fast Fourier transform, empirical mode decomposition or wavelets for the frequency estimation in one shot? *J. Sens. Sens. Syst.* **2023**, *12*, 247–260. doi:10.5194/jsss-12-247-2023.

[4] Liu, X.; et al. A highly sensitive and high-resolution resonant MEMS electrostatic field microsensor based on electrostatic stiffness perturbation. *Micromachines* **2023**, *14*, 1489. doi:10.3390/mi14081489.

[5] Qin, L.; Shen, D.; Wei, T.; Tan, Q.; Luo, T.; Zhou, Z.; Xiong, J. A wireless passive LC resonant sensor based on LTCC under high-temperature/pressure environments. *Sensors* **2015**, *15*, 16729–16739. doi:10.3390/s150716729.

[6] Gill, W. A.; Howard, I.; Mazhar, I.; McKee, K. A review of MEMS vibrating gyroscopes and their reliability issues in harsh environments. *Sensors* **2022**, *22*, 7405. doi:10.3390/s22197405.

[7] Takens, F. Detecting strange attractors in turbulence. In *Dynamical Systems and Turbulence, Warwick 1980*; Rand, D.; Young, L.-S., Eds.; Springer: Berlin, Germany, 1981; Volume 898, pp. 366–381.

[8] Fiacchini, M.; Millerioux, G. Dead-beat functional observers for discrete-time LPV systems with unknown inputs. *IEEE Trans. Autom. Control* **2013**, *58*, 3230–3235. doi:10.1109/TAC.2013.2261712.

[9] Casdagli, M.; Eubank, S.; Farmer, J. D.; Gibson, J. State space reconstruction in the presence of noise. *Physica D* **1991**, *51*, 52–98.

[10] Lee, J. M. *Introduction to Smooth Manifolds*, 2nd ed.; Springer: New York, NY, USA, 2012.

[11] Sauer, T.; Yorke, J. A.; Casdagli, M. Embedology. *J. Stat. Phys.* **1991**, *65*, 579–616.

[12] Broomhead, D. S.; Lowe, D. Multivariable functional interpolation and adaptive networks. *Complex Syst.* **1988**, *2*, 321–355.

[13] Dash, C. S. K.; Behera, A. K.; Dehuri, S.; Cho, S. B. Radial basis function neural networks: A topical state-of-the-art survey. *Open Comput. Sci.* **2016**, *6*, 33–63. doi:10.1515/comp-2016-0005.

[14] Stark, J. Invariant graphs for forced systems. *Physica D* **1997**, *109*, 163–179. doi:10.1016/S0167-2789(97)00167-X.

[15] Bernard, P. *Observer Design for Nonlinear Systems*; Ph.D. Thesis, PSL Research University, Paris, France, 2017.

[16] Lunze, J. *Linear Output Regulation–A Summary*; Edition MORA: Aachen, Germany, 2021.

[17] AVX Corporation. *C0G (NP0) Dielectric: Technical Data Sheet*; AVX Corporation, 2015. Available online: https://www.farnell.com/datasheets/81357.pdf